ACS APPLIED MATERIALS & INTERFACES

Research Article

www.acsami.org

Conductance Control in VO_2 Nanowires by Surface Doping with Gold Nanoparticles

Gil-Ho Kim,*[,†] Youngreal Kwak,[†] Inyeal Lee,[†] Servin Rathi,[†] Jeong Min Baik,[‡] and Kyung Soo Yi[§]

[†]School of Electronic and Electrical Engineering and Sungkyunkwan Advanced Institute of Nanotechnology (SAINT), Sungkyunkwan University, Suwon 440-746, Republic of Korea

[‡]School of Mechanical and Advanced Materials Engineering, Ulsan National Institute of Science and Technology (UNIST), Ulsan 689-805, Republic of Korea

[§]Department of Physics, Pusan National University, Busan 609-735, Republic of Korea

ABSTRACT: The material properties of semiconductor nanowires are greatly affected by electrical, optical, and chemical processes occurring at their surfaces because of the very large surface-to-volume ratio. Precise control over doping as well as the surface charge properties has been demonstrated in thin films and nanowires for fundamental physics and application-oriented research. However, surface doping behavior is expected to differ markedly from bulk doping in conventional semiconductor materials. Here, we show that placing gold nanoparticles, in controlled manner, on the surface of an insulating vanadium dioxide nanowire introduces local charge carriers in the nanowire, and one could, in principle, completely and continuously alter the material properties of the nanowire and obtain any intermediate level of conductivity. The current in the nanowire increased by nearly 3 times when gold nanoparticles of 10^{11} cm^{-2} order of density were controllably placed on the nanowire surface. A strong quadratic space-charge limited (SCL) transport behavior was also observed from the conductance curve suggesting the formation of two-dimensional (2D) electron-gas-like confined layer in the nanowire with adsorbed Au NPs. In addition to stimulating scientific interest, such unusual surface doping phenomena may lead to new applications of vanadium dioxide-based electronic, optical, and chemical sensing nanodevices.

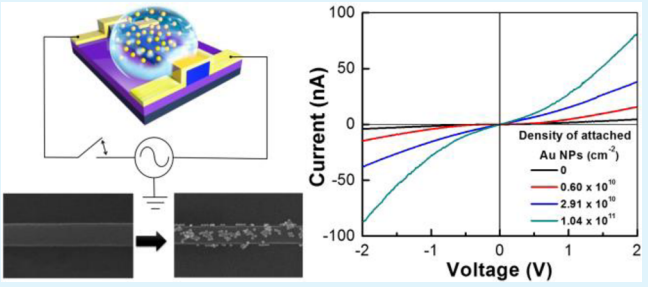

KEYWORDS: *vanadium dioxide, nanowires, dielectrophoresis, gold nanoparticles, surface-doping*

1. INTRODUCTION

Vanadium dioxide (VO_2) has attracted much attention as a strongly correlated electron material exhibiting a metal−insulator transition (MIT),[1−4] which depends upon electrical, optical, or thermal perturbations, giving rise to wide potential applications.[5−7] The applications of VO_2-based materials can be furthered by the integration of metallic, magnetic, or biomaterial nanoparticles (NPs),[8−10] which improve the functionality of the material by altering its properties. Besides giving chemical functionality to the hybrid system which can have sensing applications, NPs can also modulate the electrical conductivity of the nanowire (NW) depending upon the chemical potential difference between the NP and NW. However, the deposition of NPs on NWs is routinely done by chemical or thermal/e-beam deposition methods, where the control of NP density is the critical issue and hard to achieve. The controlled deposition of NPs would not only lead to desired conductivity but can also have wide application to other areas including biomedical, photonic sensing where the properties are dependent upon the NP density. However, until recently, it has been difficult to accurately pack a sufficient number of metal NPs onto a nanowire (NW) surface.

In this work, we demonstrate a new method that enables the assembly of Au NPs on VO_2 NWs using an alternating current (ac) dielectrophoresis (DEP) process.[11−14] The DEP parameters were controlled to assemble a different number of Au NPs on the VO_2 NW. We investigated and optimized key experimental parameters to control the conductance of the VO_2 NWs via the DEP process. We also simulated the DEP process and found that the simulation results supported experimental observations.

2. EXPERIMENTAL SECTION

VO_2 Nanowire Growth and Device Fabrication. Single-crystal VO_2 nanowires (NWs) with axial growth direction preferentially oriented along [100] were grown by physical vapor deposition at atmospheric pressure without the use of any catalyst. Initially, 0.1 g of fine mesh VO_2 (99.9%, Aldrich) powder was placed at the center of a 10 cm long quartz boat, and a precleaned SiO_2/Si substrate was located approximately 5 mm from the VO_2 powder. The quartz boat was then placed at the center of a quartz tube furnace, and high-purity

Received: February 14, 2014
Accepted: August 20, 2014
Published: August 20, 2014

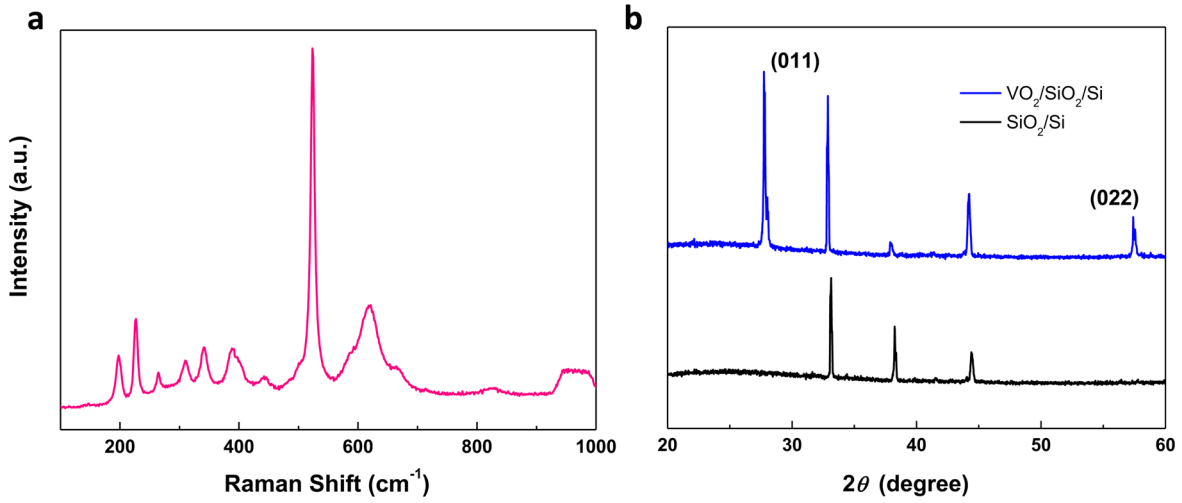

Figure 1. (a) Raman spectra and (b) X-ray diffraction (XRD) patterns of as-grown VO_2 NW on a SiO_2/Si substrate.

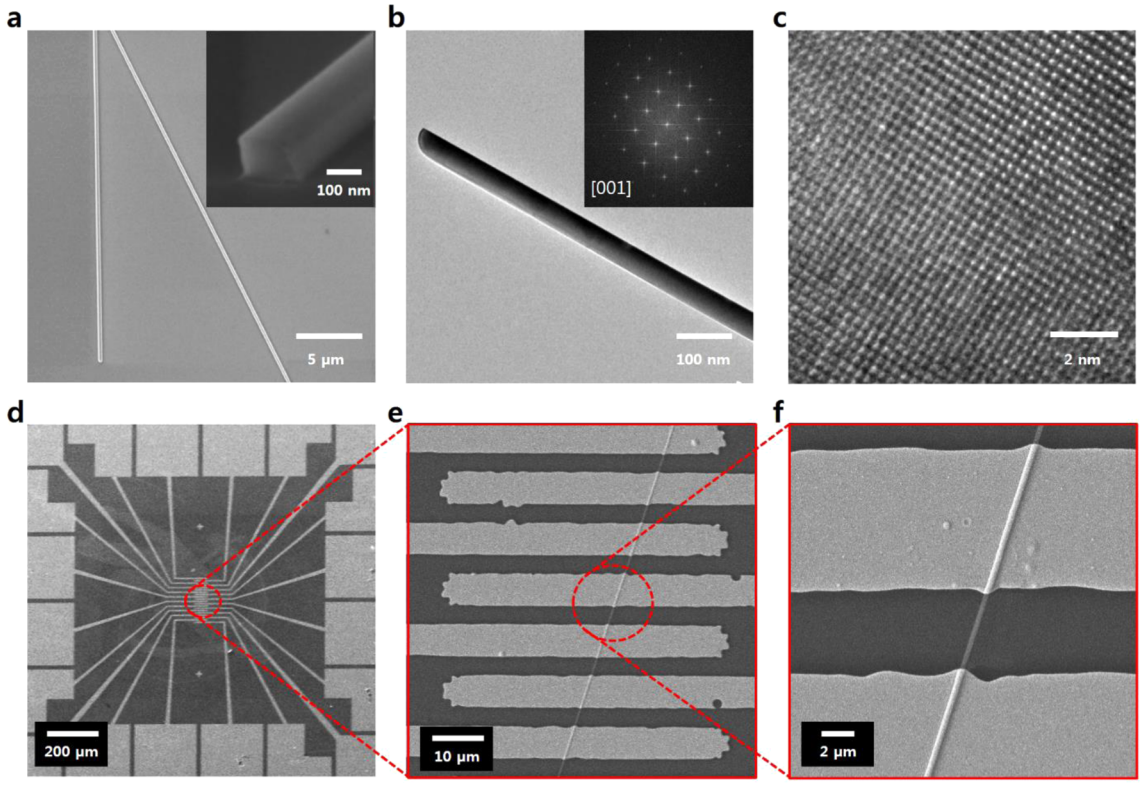

Figure 2. SEM and TEM images of a VO_2 NW and a chip. (a) SEM image of a VO_2 NW grown on a SiO_2/Si substrate. Inset shows rectangular cross section of the VO_2 NW morphology. (b) TEM image of a VO_2 NW. Inset shows nanobeam diffraction pattern. (c) High-resolution TEM image of a VO_2 NW tip. (d) Full image of a chip showing 20 parallel electrodes with individual contact pads. (e) Magnified view of seven electrodes on the 150 μm long VO_2 NW. (f) Magnified view showing the VO_2 NW with a mean width of 220 nm between two electrodes with a gap of 4 μm.

He carrier gas (99.999%) was injected through the furnace at 300 sccm. The furnace temperature was increased to approximately 700 °C, and the sample growth was allowed to proceed for 2 h. After the growth, the samples were allowed to cool down to room temperature in flowing He before removing the substrate covered with NWs from the furnace. From X-ray diffraction and Raman measurements in Figure 1, we confirmed that the nanowires were single crystalline monoclinic VO_2. Raman peaks at 197, 227, 264, 311, 342, 396, 443, and 614 cm^{-1} are the indication of the monoclinic phase whereas the peak at 524 cm^{-1} is from the background SiO_2/Si substrate. XRD reflection at (011) and (022) indicates preferential growth directions and corresponds to a monoclinic lattice while the peak at 33.2° is from the SiO_2/Si substrate. The nanowire width and height, measured at the nanowire−SiO_2 interface for a representative number of nanowires, was determined by scanning electron microscopy (SEM) as 100−400 (±10) nm and 50−200 (±5) nm, respectively. The lengths of most of the nanowires were in the range 20−150 μm.

For device fabrication, the grown VO_2 NWs were detached from the SiO_2 substrate and dispersed onto another substrate 300 nm in thickness consisting of SiO_2 and p-type Si. The Au electrodes used in this work were fabricated using standard optical lithography. After developing the pattern, a metal-stack deposition, consisting of Ti/Au (10/200 nm), was carried out in high vacuum e-beam deposition system, which is followed by lift-off in acetone. Finally, thermal

dx.doi.org/10.1021/am504229n | ACS Appl. Mater. Interfaces 2014, 6, 14812−14818

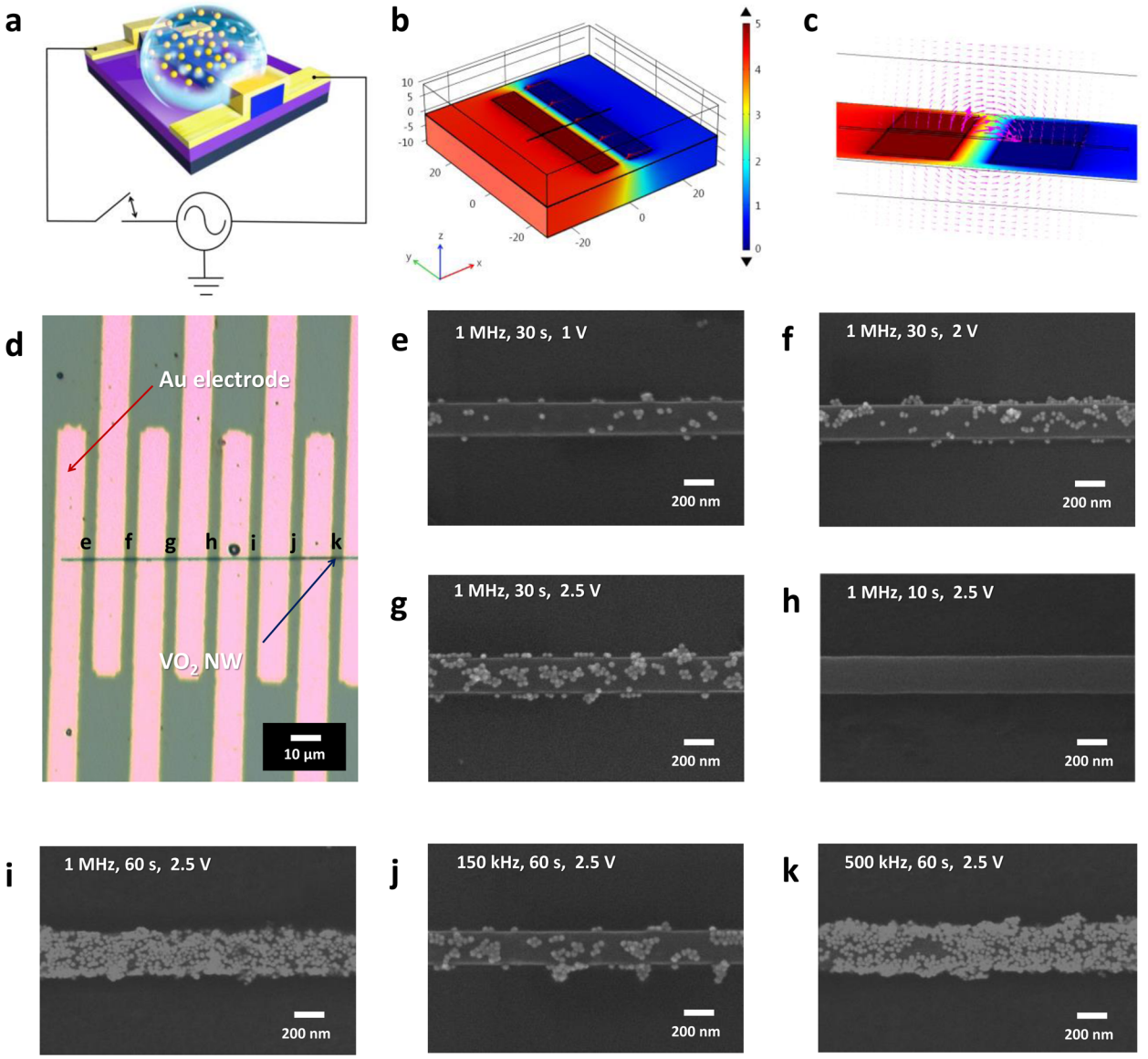

Figure 3. Schematic view of the experimental setup used for the (a) ac DEP, (b and c) the electric potential and field profiles around a VO_2 NW, and the Au NPs assembled on the surface of the VO_2 NW. (d) SEM images of a sample with patterned electrodes and a VO_2 NW. DEP was carried out (e−g) for 30 s at a fixed frequency of 1 MHz by applying voltages of 1, 2, and 2.5 V; (g−i) at a fixed frequency of 1 MHz by applying a peak-to-peak voltage of 2.5 V for 30, 10, and 60 s; (i−k) by applying a fixed applied peak-to-peak voltage of 2.5 V for 60 s at frequencies of 1 MHz, 150 kHz, and 500 kHz.

annealing at 200 °C for 1 min was done to ensure good Ohmic contacts between the metal and VO_2 NW. The separation between the Au electrodes was 4 μm, and a single chip contained 20 such electrodes.

VO_2 Nanowire Characterization and Measurement Details. Field-emission scanning electron microscopy (SEM) was used to image the VO_2 nanowires after the growth, when patterned on chip and finally when DEP-processed with Au NPs. The high-resolution transmission electron microscopy (TEM) images were collected using a Cs-corrected JEM-2100 operated at 200 kV. Besides the SEM images, energy-dispersive X-ray spectroscopy was also used to confirm the exclusive composition of the VO_2 NW decorated only with Au NPs. Tektronix AFG3102 function generator and TDS3052C oscilloscope were used for DEP process. The $I-V$ characteristics were measured using Lock-in Amplifier and Kethley dc voltage source with Oxford system for low temperature measurement.

3. RESULTS AND DISCUSSION

Figure 2a−c shows the morphology and crystallinity determined by scanning electron microscopy (SEM) and transmission electron microscopy (TEM) images. The atomic image and patterns shown as distinct spots in Figure 1b clearly indicate highly crystalline properties of the VO_2 nanowires. Figure 2d−f shows the detailed images of the chip pattern used in this study. Figure 3a shows a schematic of the experimental setup used for the ac DEP assembly, consisting of a function generator connected directly through the chip to the oscilloscope. The DEP force generally depends strongly on the distribution and frequency of the ac electric field. In the presence of a nonuniform external electric field, spherical Au NPs floating in deionized water become electrically polarized, each with an induced electric dipole moment $\vec{p}$.[15] The inhomogeneous electric field forces the polarized Au NPs to move in the direction of the higher electric field, in which the

VO_2 NW is located and causes mutual attraction between the VO_2 NW and Au NPs, giving rise to the assembly of the Au NPs on the surface of the VO_2 NW.[15] Figure 3b,c shows simulated spatial profiles of the electric potential $V(x,y,z)$ and the corresponding electric field $\vec{E}$ near the VO_2 NW in our DEP environment; these images were obtained using the COMSOL Multiphysics package.[16] The simulation settings applied were as follows. A pair of coplanar Au electrodes was separated by 4 μm. The electric potential was applied to the left-hand electrode, and the right-hand electrode was grounded. The relative permittivities of the deionized water, Au electrodes, 300 nm thick SiO_2 film, Si substrate, and 220 nm wide VO_2 NW were set at 80, −1000, 3.9, 11.7, and 36, respectively. The solver adopted automatic meshing of the device structure for accurate results.

In Figure 3c, a sliced view of the potential profile is shown in the $x-y$ plane in which the coplanar electrodes were located. The arrows in Figure 3c denote the local electric field ($\vec{E}$) below and above the $x-y$ plane around the device. The simulation results demonstrated that a highly inhomogeneous electric field was formed around the VO_2 NW between the electrodes (unlike the uniform electric field between parallel electrodes in conventional devices). The electric field was stronger near the edges of a pair of charged electrodes and was relatively reduced near the VO_2 NW placed between the electrodes. The electric field further decreased in magnitude at greater distances from the NW.

It is important to control the density of the Au NPs in order to obtain a consistent and reliable Au NP assembly at the surface of the VO_2 NW. This was done by varying three key DEP parameters, i.e., the frequency f, amplitude of the applied ac voltage V_{pp}, and duration of DEP processing t. In our experiments, we controlled the density of the Au NPs by varying one parameter and keeping the other two fixed. For each set of parameters, we counted the density of NPs assembled on the VO_2 NW surface. Figure 3d–k shows the SEM images of the Au NP assemblies of different densities on a specific VO_2 NW from a single chip. Figure 3d shows the SEM image of the Au electrodes used in this work, which were 10 μm wide with a gap of 4 μm. Figure 3e–g shows the assemblies obtained with three different V_{pp} values at a fixed frequency and time of 1 MHz and 30 s, respectively. For larger values of V_{pp}, the density of the Au NPs on the VO_2 NW also increased. The SEM images after DEP at V_{pp} = 1.0, 2.0, and 2.5 V showed Au NP densities of 6.0×10^9, 2.3×10^{10}, and 2.9×10^{10} cm^{-2}, respectively. At V_{pp} = 3 V, the VO_2 NW burned and disappeared owing to Joule heating. The current suddenly increased when the Au NPs fully covered the VO_2 NW. Figure 3g–i shows the wires obtained by carrying out DEP for t = 30, 10, and 60 s at f = 1 MHz and V_{pp} = 2.5 V. Figure 3i–k shows the frequency dependence of the Au NPs assembled at V_{pp} = 2.5 V; t = 60 s; and f = 1 MHz, 150 kHz, and 500 kHz. As the frequency increased to up to 1 MHz, the assembly of the Au NPs at the VO_2 NW surface increased steadily. However, if DEP proceeded for longer time, it can result in drying of the solution droplet which limits the nanoparticle attaching on the nanowire, or for large droplets, it can also sometimes shunt the nanowire, both of which are highly undesirable conditions. Therefore, nanoparticle solution droplets and DEP time are optimized so as to avoid these conditions in the experiment.

SEM images in Figure 3e–k and the energy-dispersive X-ray spectrum (Figure 4) confirm the assembly of the Au NPs assembled on the surface of a VO_2 NW. The attached Au NPs

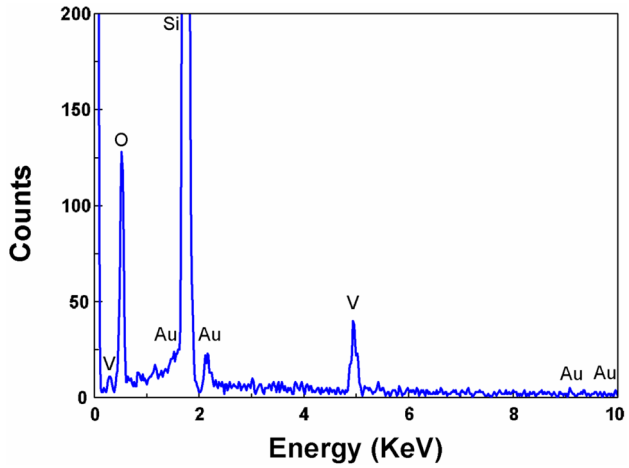

Figure 4. Energy-dispersive X-ray spectrum of Au NPs assembled on the surface of a VO_2 NW showing peaks corresponding to Au and V. Si and O peaks are attributed to the substrate (SiO_2/Si).

were counted directly from Figure 3e–k. The NPs in direct contact with the NW were considered, and the particles aggregated onto the top of the contacted NPs were excluded. Table 1 tabulates the density of the NPs, calculated by considering the rectangular cross section of the VO_2 NW with a width of 210 nm and height of 105 nm, for different DEP voltage values. However, with the 3D topology of the NW, this method of counting from the 2D topography of NW is bound to have some error margins. Therefore, the deposition procedure has been carried out many times on several samples; on the basis of the experimental data and with the counting-method limitation, a variation of up to 10% has been observed in the deposited density of NPs on the NW.

Table 1. Number of Au NPs Trapped on the Surface of the Undoped VO_2 NW at the Applied Frequency, Time, and Peak-to-Peak Voltage Values in Figure 3e–k

	no. of Au NPs trapped on the VO_2 NW surface	
DEP conditions for each panel in Figure 2e–k	count	density [cm^{-2}] ± 10%
(e) 1 MHz, 30 s, 1 V	40	6.0×10^9
(f) 1 MHz, 30 s, 2 V	154	2.3×10^{10}
(g) 1 MHz, 30 s, 2.5 V	194	2.9×10^{10}
(h) 1 MHz, 10 s, 2.5 V	0	0
(i) 1 MHz, 60 s, 2.5 V	695	1.0×10^{11}
(j) 150 kHz, 60 s, 2.5 V	140	2.1×10^{10}
(k) 500 kHz, 60 s, 2.5 V	485	7.3×10^{10}

The current–voltage ($I-V$) curves in Figure 5a,b show symmetric nonlinear semiconducting behavior even at a bare undoped VO_2 NW. The electrical current at Au NP density of 1.0×10^{11} cm^{-2} was about 80 nA at 2 V, which is about a 20-time increase when compared with that of the bare VO_2 NW. The increase in current could be attributed to the enhanced number of carriers in the VO_2 NW due to the attached Au NPs. It may be noted that the conductivity modulation is observed in VO_2 NWs well below the MIT temperature (68 °C) as the carrier density in NW in metallic state reaches 10^{23} cm^{-3} from 10^{16} cm^{-3} in the insulating state; at such high carrier concentration, the modulation from Au NPs is ineffective and can be ruled out. However, this Au NP deposition can influence

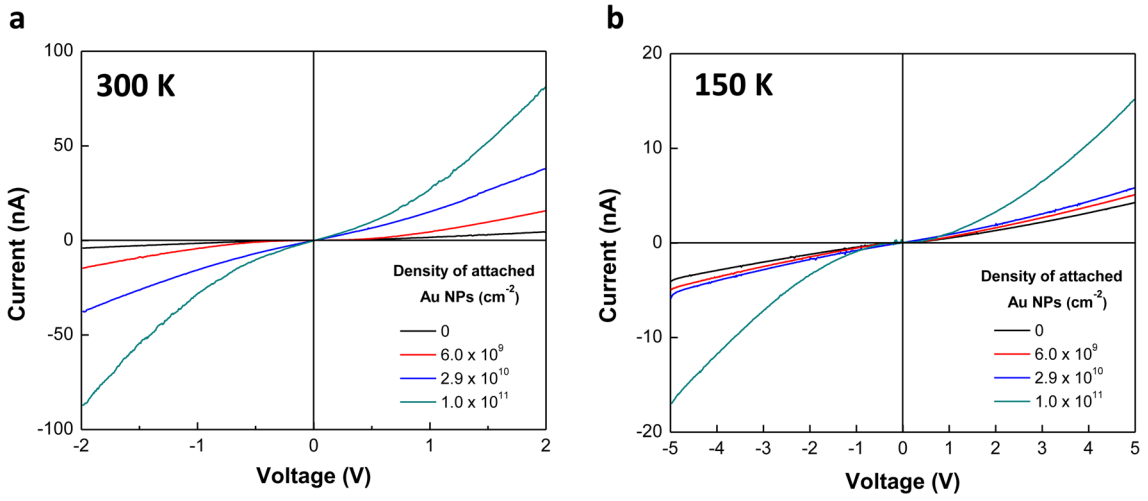

Figure 5. Transport properties of the VO_2 NW–Au NP assembly at various Au NP densities. I–V characteristics of the VO_2 NW for four different Au NP densities at (a) 300 K and (b) 150 K.

the MIT temperature as per Mott's transition criteria which depend upon the critical strength of electron-density-dependent screening of carriers. This effect of Au NPs on MIT point in NWs is out-of-scope in the present work and would be studied separately. The conductance variation with NP density at both 300 and 150 K is plotted in Figure 6. It can be seen from the

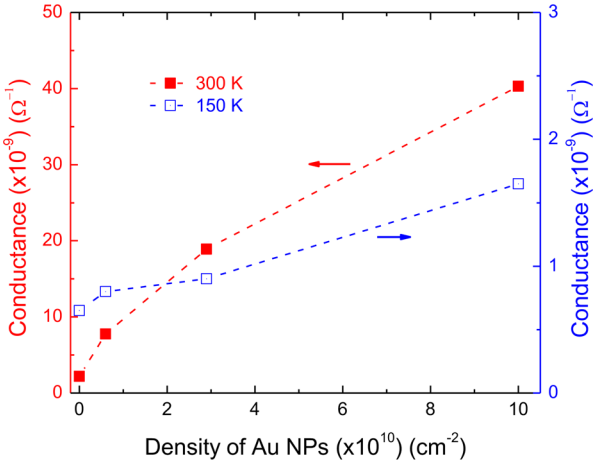

Figure 6. Conductance variation with NPs density at 300 and 150 K plotted in red and blue square symbols, respectively.

figure that the conductance variations are much more pronounced at 300 K than at 150 K. This may be due to the decrease in the concentration of thermally activated carriers in NW which can give rise to the localization of the carriers around NPs and may also result in hopping conduction at 150 K. However, the effect of NPs on conductance modulation of NW can still be seen clearly which indicates that the carrier-doping from NPs to NW is not affected by the temperature variation as the drop in the pristine NW current is followed by the other NP deposited NWs at 150 K.

The surface doping effect of the Au NP can be visualized through Figure 7, which shows the schematic overview of the Au NPs–VO_2 NW assembly and its energy band alignment before and after contact. Figure 7a,b shows a schematic view of charge transfer occurring during the assembly of the VO_2 NW and Au NPs and illuminates the space charge distribution at the NP–NW interface. The attached Au NPs, acting as a dopant material, provide mobile carriers to the VO_2 NW. Figure 7c–e, which illustrates the energy band alignments before and after contact between the Au NP and the VO_2 NW, have been obtained by employing a model of metal–semiconductor junctions. In this model, the metal exhibits the lower work function.[17] Figure 7c–e shows the alignments of the individual energy bands of the VO_2 NW and Au NP before and after contact.

In this study, we used Au NPs that were 20 nm in diameter. These NPs were not small enough to reveal quantized energy levels of the carriers at room temperature. Therefore, they are not subject to the quantum confinement effect, which is expected to divulge even at room temperature in Au NPs of diameters smaller than 5 nm.[18] The energy gap between the conduction and valence bands of VO_2 is ~0.5 eV, and the work function, which is the difference between the vacuum level and the Fermi level of the material, is ~5.15 eV. The typical bulk work function of Au is ~4.83 eV. After contact, the Fermi levels of the VO_2 NW and the Au NP were aligned by transfer of electrons from the metal NPs to the insulator NW (Figure 7e). At the junction of the Au NPs and the VO_2 NW, the Au NP and VO_2 NW sides are positively and negatively charged, respectively. Because Au is a noble metal with a high free carrier concentration ($\sim 10^{22}$ cm^{-3}), a negligible depletion region appears on Au, whereas surface accumulation of electrons on the VO_2 NW side results in the formation of 2D surface channel.

From the above discussion, we conjecture that a thin electron accumulation layer is formed in the VO_2 NW by surface carrier injection through the Au NPs attached by DEP,[15] and carrier conduction occurs through the effectively "two-dimensional" (2D) surface channel around the insulating core of the NW (see Figure 7b). The Ohmic contribution to the surface current density in a weakly biased channel of length L (=4 μm) is given by $J_\Omega = e\mu n_{2D}V/L$, where e, μ, and n_{2D} denote the elementary charge, effective charge carrier mobility, and 2D carrier density, respectively. The nonlinear symmetric characteristic, as shown in Figure 5a,b, is a signature of space-charge limited (SCL) current,[19,20] where the SCL current density in a highly biased thin layer is written as[20] $J_{SCL} = (2\varepsilon_0\epsilon_r\mu/\pi)(V^2/L^2)$, where ε_0

dx.doi.org/10.1021/am504229n | ACS Appl. Mater. Interfaces 2014, 6, 14812–14818

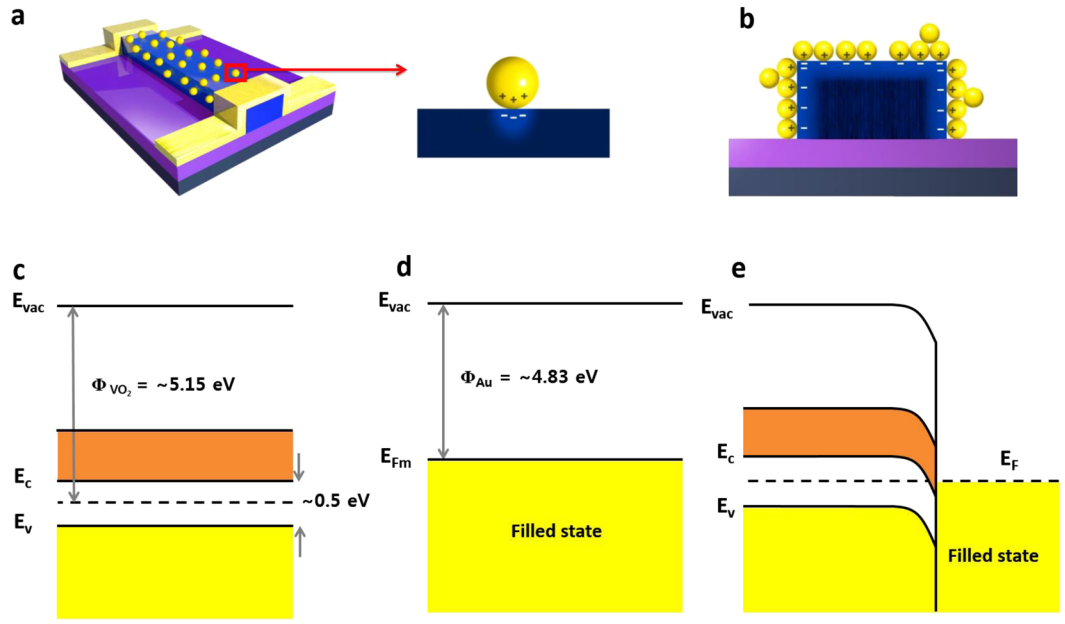

Figure 7. Assembly of Au NPs on a VO_2 NW and energy band alignment before and after contact between the Au NP and VO_2 NW. (a) Schematic view of charge transfer during the assembly of Au NPs on VO_2 NW. Before attachment, the Au NP and VO_2 NW are not charged. After attachment, the Au NP is positively charged, and the VO_2 NW is negatively charged; hence, the undoped VO_2 NW becomes conducting. (b) Schematic cross section of VO_2 NW with adsorbed Au NPs. A shell of negatively charged conducting region surrounds the insulating core region of the VO_2 NW. The area of the NW contributing to charge conduction is smaller than the physical area. (c and d) Band edges of the VO_2 NW and Au NP before contact. (e) Band alignment at the heterointerface of the VO_2 NW and Au (in equilibrium). The Fermi level is pinned at the defect states of VO_2. The amount of downward band edge bending at the contact is given by the difference of the work functions of the NP and the NW.

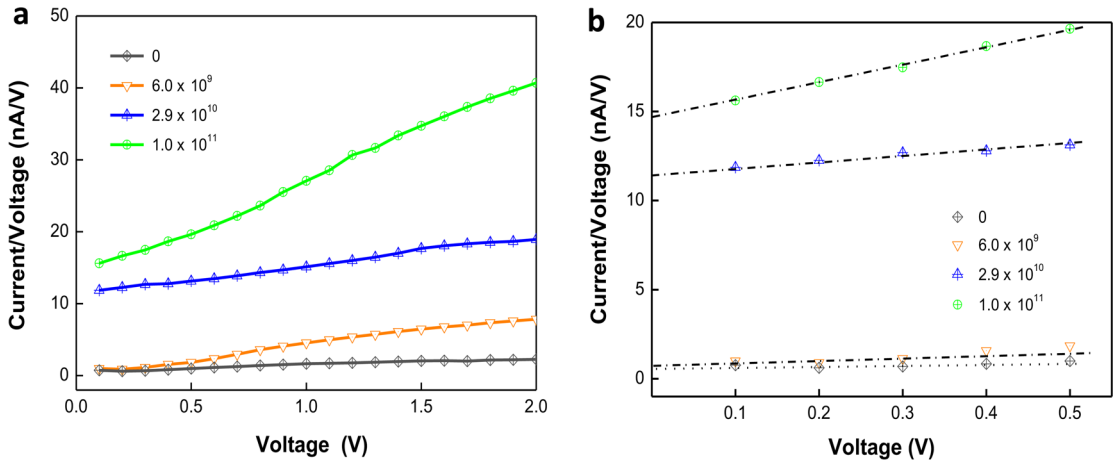

Figure 8. Plots of I/V (current/voltage) as a function of voltage (a) at 300 K for the result shown in Figure 5a. (b) Magnification of the I/V versus V behavior in the low-voltage region at 300 K. Each broken line serves as a guide to the eye for the y-intercept and slope for a particular density of DEP attached Au NPs.

and ϵ_r are the electric permittivity of vacuum and the relative permittivity of the NW, respectively.

In Figure 8a, I/V is displayed as a function of V for the results obtained at T = 300 K, shown in Figure 5a. The y-intercept, illustrated in Figure 8b, and slope of the I/V versus V plot designate the Ohmic and SCL contributions, respectively. In addition to the linear Ohmic contribution, we observe a strong quadratic SCL transport behavior in our VO_2 NWs consisting of DEP adsorbed Au NPs on the surface. We understand that the strong SCL behavior in our VO_2 NW is a direct consequence of the poor electrostatic screening of the injected carriers in the high aspect ratio (~2.5×10^{-2}) VO_2 NWs. The cross over voltage (V_c) from the Ohmic region at low bias to the SCL regime at high bias regions allows us to write n_{2D} as $n_{2D} = (2\varepsilon_0\epsilon_r\pi e)(V_c/L)$. For the cases shown in Figure 5a, the values of V_c are 1.47, 3.8, 0.4, and 0.2 V, respectively, at 300 K.

The corresponding effective surface carrier densities for the VO_2 NWs were found to be $n_{2D} \sim 6.3 \times 10^{10}/cm^2$ to $1.2 \times 10^{12}/cm^2$ at 300 K. The charge carrier mobility could also be estimated from the $I-V$ curve by applying the relationship $\mu_{SCL} = (\pi/2\varepsilon_0\epsilon_r)((JL^2)/(V^2))$. Our results obtained at room temperature yield μ_{SCL} values in the range ~5.6–37.6 $cm^2/(V\,s)$, at the cross over voltages. The values were an order of magnitude larger than that shown by typical semiconducting VO_2[21] and were of the same order of magnitude as that shown by the mobility of metallic VO_2. In obtaining these numerical

dx.doi.org/10.1021/am504229n | ACS Appl. Mater. Interfaces 2014, 6, 14812–14818

values, we used ϵ_r = 36 and the fact that the DEP attached Au NPs were located on the top and two side faces of the VO_2 NW with width of 210 nm and thickness of 105 nm (see Figure 2b). Our observation indicated that the DEP processed Au NP–VO_2 NW assembly possessed superior electrical properties at room temperature.

4. CONCLUSION

In conclusion, we have demonstrated the assembly of Au NPs on a VO_2 NW using ac DEP. The Au NP density on the surface of the VO_2 NW could be accurately controlled by varying three parameters, i.e., f, V_{pp}, and t, of the DEP process. The VO_2 NW with trapped Au NPs exhibited stable transport behavior that is typical of doped semiconductor material because the Au NPs provided negative charge carriers to the undoped insulating VO_2 NW. This intelligent hybrid system might have tremendous potential for realizing various smart nanoscale field-effect transistors, optoelectronic switches, and miniaturized biochemical and gas sensors for myriad applications.

AUTHOR INFORMATION

Corresponding Author

*E-mail: ghkim@skku.edu.

Notes

The authors declare no competing financial interest.

ACKNOWLEDGMENTS

This research was supported by Basic Science Research Program through the National Research Foundation of Korea (NRF) funded by the Ministry of Education, Science and Technology (Grants 2013R1A2A2A01069023 and 201306330002). We acknowledge helpful discussions with Professor Martin Moskovits and Dr. Chris Ford.

REFERENCES

(1) Morin, F. J. Oxides Which Show a Metal-to-Insulator Transition at the Neel Temperature. *Phys. Rev. Lett.* **1959**, *3*, 34–36.
(2) Goodenough, J. B. The Two Components of the Crystallographic Transition in VO_2. *J. Solid State Chem.* **1971**, *3*, 490–500.
(3) Imada, M.; Fujimori, A.; Tokura, Y. Metal-Insulator Transitions. *Rev. Mod. Phys.* **1998**, *70*, 1039–1263.
(4) Basov, D. N.; Averitt, R. D.; Marel, D.; Dressel, M.; Haule, K. Electrodynamics of Correlated Electron Materials. *Rev. Mod. Phys.* **2011**, *83*, 471.
(5) Nakano, M.; Shibuya, K.; Okuyama, D.; Hatano, T.; Ono, S.; Kawasaki, M.; Iwasa, Y.; Tokura, Y. Collective Bulk Carrier Delocalization Driven by Electrostatic Surface Charge Accumulation. *Nature* **2012**, *487*, 459–462.
(6) Seo, M.; Kyoung, J.; Park, H.; Koo, S.; Kim, H. S.; Bernien, H.; Kim, B. J.; Choe, J. H.; Ahn, Y. H.; Kim, H. T.; Park, N.; Park, Q. H.; Ahn, K.; Kim, D. S. Active Terahertz Nanoantennas Based on VO_2 Phase Transition. *Nano Lett.* **2010**, *10*, 2064–2068.
(7) Zimmers, A.; Aigouy, L.; Mortier, M.; Sharoni, A.; Wang, S.; West, K. G.; Ramirez, J. G.; Schuller, I. K. Role of Thermal Heating on the Voltage Induced Insulator-Metal Transition in VO_2. *Phys. Rev. Lett.* **2013**, *110*, 56601.
(8) Hu, M. S.; Chen, H. L.; Shen, C. H.; Hong, L. S.; Huang, B. R.; Chen, K. H.; Chen, L. C. Photosensitive Gold-Nanoparticle-Embedded Dielectric Nanowires. *Nat. Mater.* **2006**, *5*, 102–106.
(9) Puntes, V. F.; Gorostiza, P.; Aruguete, D. M.; Bastus, N. G.; Alivisatos, A. P. Collective Behaviour in Two-Dimensional Cobalt Nanoparticle Assemblies Observed by Magnetic Force Microscopy. *Nat. Mater.* **2004**, *3*, 263–268.
(10) Tan, S. J.; Campolongo, M. J.; Luo, D.; Cheng, W. Building Plasmonic Nanostructures with DNA. *Nat. Nanotechnol.* **2011**, *6*, 268–276.
(11) Gascoyne, P. R. C.; Vykoukal, J. Particle Separation by Dielectrophoresis. *Electrophoresis* **2002**, *23*, 1973–1983.
(12) Gierhart, B. C.; Howitt, D. G.; Chen, S. J.; Smith, R. L.; Collins, S. D. Frequency Dependence of Gold Nanoparticle Superassembly by Dielectrophoresis. *Langmuir* **2007**, *23*, 12450–12456.
(13) Hermanson, K. D.; Lumsdon, S. O.; Williams, J. P.; Kaler, E. W.; Velev, O. D. Dielectrophoretic Assembly of Electrically Functional Microwires from Nanoparticle Suspensions. *Science* **2001**, *294*, 1082–1086.
(14) Cheon, D.; Kumar, S.; Kim, G. H. Assembly of Gold Nanoparticles of Different Diameters between Nanogap Electrodes. *Appl. Phys. Lett.* **2010**, *96*, 013101.
(15) Pohl, H. A. *Dielectrophoresis*; Cambridge University Press: Cambridge, U.K., 1978.
(16) Multiphysics Modeling and Simulation Software (COMSOL AB ver. 4.1) was used for our simulations (www.comsol.com).
(17) Xu, G.; Huang, C. M.; Tazawa, M.; Jin, P.; Chen, D. M.; Miao, L. Electron Injection Assisted Phase Transition in a Nano-Au-VO_2 Junction. *Appl. Phys. Lett.* **2008**, *93*, 061911.
(18) Yi, K. S.; Trivedi, K.; Floresca, H. C.; Yuk, H.; Hu, W.; Kim, M. J. Room-Temperature Quantum Confinement Effects in Transport Properties of Ultrathin Si Nanowire Field-Effect Transistors. *Nano Lett.* **2011**, *11*, 5465–5470.
(19) Talin, A.; Leonard, F.; Swartzentruber, B. S.; Wang, X.; Hersee, S. Unusually Strong Space-Charge-Limited Current in Thin Wires. *Phys. Rev. Lett.* **2008**, *101*, 076802.
(20) Geurst, J. A. Theory of Space-Charge-Limited Currents in Thin Semiconductor Layers. *Phys. Status Solidi B* **1966**, *15*, 107–118.
(21) Maeng, J.; Kim, T. W.; Jo, G.; Lee, T. Fabrication, Structural and Electrical Characterization of VO_2 Nanowires. *Mater. Res. Bull.* **2008**, *43*, 1649–1656.